第 32卷 第 1期 焊 接 学 报 Vol.32 No.1
2011年 1月 TRANSACTIONS OF THE CHINA WELDING INSTITUTION January 2011

等离子熔覆 TiC/Fe-Cr金属陶瓷复合涂层

刘均海[1,2], 黄继华[1], 刘均波[3], 宋桂香[4]

(1. 北京科技大学 材料学院, 北京 100083; 2. 威海职业学院 机电工程系, 山东 威海 264210; 3. 潍坊学院机电工程系, 山东 潍坊 261041; 4. 威海职业学院 技能实训中心, 山东 威海 264210)

摘 要: 以钛铁粉、高碳铬铁粉、硼铁粉、硅铁粉等为原料, 利用等离子熔覆技术在 Q235钢表面原位反应合成了与基材冶金结合 TiC/Fe-Cr金属陶瓷复合涂层. 利用 SEM, XRD和 EDS等分析了涂层的显微组织, 并在室温干滑动磨损条件下测试了该涂层的耐磨性能. 结果表明, 涂层组织由 TiC相、初生相 Cr_7C_3、共晶 $(Cr, Fe)_7C_3$ 和奥氏体构成. 利用等离子熔覆技术原位合成的 TiC相呈现颗粒状、棒状和树枝状等形态. 涂层具有较高的硬度和优异的耐磨性.

关键词: 等离子熔覆; TiC; Cr_7C_3; 涂层; 原位合成

中图分类号: TG115 文献标识码: A 文章编号: 0253-360X(2011)01-0093-04

刘均海

0 序 言

熔覆技术是指采用激光束、电子束或离子束等高能束在选定工件表面熔覆一层特殊性能的材料, 以改善其表面性能的工艺[1]. 等离子熔覆技术可在金属表面获得合金以及金属间化合物复合涂层, 已广泛应用于电力、煤炭、冶金、机械等诸多工业领域, 成为现代表面工程技术的一个研究热点[2-5].

Cr_7C_3 金属陶瓷具有硬度高、耐腐蚀性及抗氧化性好等优点, 常被用作耐磨、抗氧化和耐腐蚀涂层的增强相[6,7]. TiC颗粒具备硬度高、熔点高、热稳定性好等特点, 而且可以通过钛粉或 TiFe粉与碳反应合成. 近年来对制备 TiC颗粒增强金属基复合材料的研究成为热点. TiC在复合材料中多以微细颗粒析出, 呈弥散分布, 对基体金属的韧性损害较小. TiC颗粒增强的复合材料涂层增强了零件的表面强度和综合性能[8-10].

文中以高碳铬铁粉与钛铁粉的混合粉作为等离子熔覆合金粉, 通过同步送粉方式送粉, 以等离子转移弧为热源制备等离子熔覆 TiC/Fe-Cr金属陶瓷复合涂层.

1 试验方法

试样材料分两部分, 一是基体, 二是合金粉末. 基材选取 Q235碳钢, 其化学成分 (质量分数, %): C ≤0.18, Mn 0.35~0.80, Si ≤0.30, S ≤0.040, P ≤0.040; 尺寸为 50 mm × 30 mm × 10 mm. 合金粉末材料选取钛铁粉、高碳铬铁粉、硅铁粉、硼铁粉等粉末, 其成分见表 1, 按照高碳铬铁粉 60%, 硼铁粉 10%, 硅铁粉 4%, 钛铁粉 26%的比例配置合金粉, 并混合均匀, 其粒度大致在 60~300目.

表 1 原料粉末化分成分 (质量分数, %)

Table 1 Chemical compositions of powders for surface alloying

粉末	Ti	Cr	B	Al	Mn	Si	C	P	S	Fe
钛铁粉	47.0	—	—	1.72	1.9	0.2	0.2	0.096	0.02	余量
高碳铬铁粉	—	62	—	0.25	—	1.62	8.0	0.03	0.04	余量
硼铁粉	—	—	19.44	0.38	—	0.47	0.42	0.042	0.002	余量
硅铁粉	—	—	—	—	0.43	45	0.38	0.021	0.009	余量

等离子熔覆设备采用 DRF-1型全自动等离子熔覆机床. 等离子熔覆工艺参数为: 工作电流 200 A, 工作电压 30 V, 送粉量 30 g/min, 扫描速度 350 mm/min, 工作气体 (Ar) 流量 2.5 L/min, 送粉气体 (Ar) 流量 3 L/min. 用 S-3400型扫描电子显微镜观察显微组织; 采用日本 Dmax-2200 PC旋转阳极 X射线衍射仪并结合 S-530型 Link ISIS能谱仪进行物相鉴定; 在 MH-6型半自动显微硬度计上进行显微硬度测量, 载荷为 1.962 N, 加载保持时间为 10 s. 试样处理分为两种, 一种无腐蚀; 一种采用氢氟酸

收稿日期: 2009-09-19

4%、硝酸 4%和水 92%的混合液腐蚀 5 min.

2 试验结果与分析

2.1 等离子熔覆 TiC/Fe-Cr 金属陶瓷复合材料涂层的显微组织分析

图 1为合金粉中钛铁粉的 X射线衍射图谱，由图 1中可以看出，原始粉末中主要相为 FeTi，没有 TiC相. 图 2为等离子熔覆金属陶瓷复合材料涂层 X射线衍射图谱，可见，涂层的主要组成相为 TiC、$(Cr,Fe)_7C_3$ 及 γ-Fe固溶体，与图 1比较，可以发现涂层中原位合成了 TiC相.

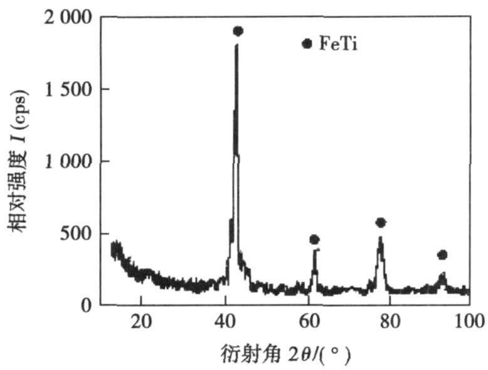

图 1 钛铁粉的 X 射线衍射结果

Fig. 1 XRD pattern of high carbon Ferrotitanium powder

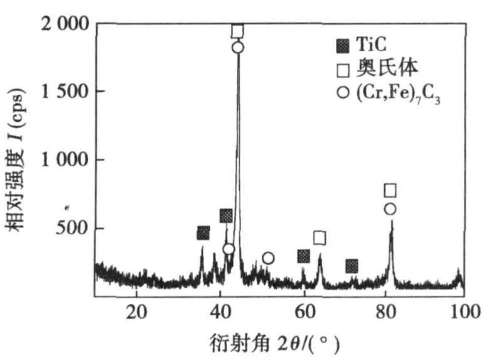

图 2 等离子熔覆涂层 X 射线衍射图谱

Fig. 2 XRD pattern of plasma clad ceramal coating

图 3为等离子熔覆复合涂层不同放大倍数下的组织结构. 从图 3a可明显看出，无显微孔洞及裂纹、夹渣等缺陷. 显微组织结构为大量的灰黑色颗粒状和树枝晶状相分布在基体上. 由图 3b可知，无腐蚀的试样高倍显微组织中有三种不同颜色的区域，即浅灰色区域、灰色区域和灰黑区域，灰黑区域约占总区域的体积比约为 21%. 由图 3c可知，显微组织区由条状组织 A、灰色块状组织 B和灰黑块状组织 C组成，对图 3c中标有 A、B和 C三种区域进行能谱分析（表 2）可知，A区 Fe 70.52%，Cr 17.03%，Ti 3.39%，C 6.41%，结合图 2等离子熔覆涂层 X射线衍射图谱可确定条状相为 $(Cr,Fe)_7C_3$ 共晶组织. B区铁含量 38.77%、铬含量 17.0%、碳含量 9.11%，可确定 B区为初生相 Cr_7C_3. 初生相 Cr_7C_3 中的铬和碳含量高于 $(Cr,Fe)_7C_3$ 共晶组织中铬和碳. C区碳、钛含量较多，其含量分别为 16.44%、78.89%（质量分数），可确定灰黑色相为 TiC相.

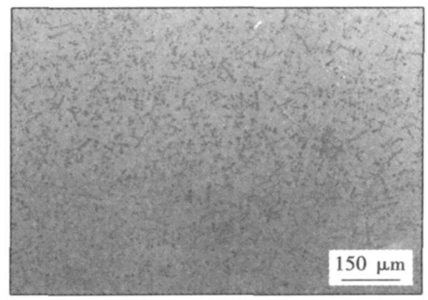

(a) 无腐蚀试样低倍形貌

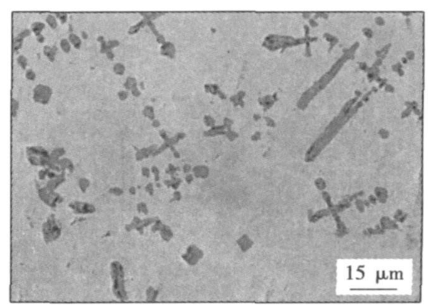

(b) 无腐蚀试样高倍形貌

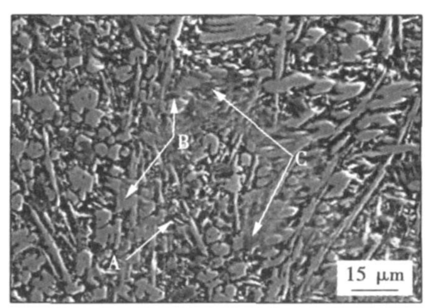

(c) 腐蚀后试样高倍形貌

图 3 等离子熔覆复合涂层显微组织 SEM形貌

Fig. 3 SEM images showing microstructure of plasma clad composite coating

由上述分析可知，等离子熔覆金属陶瓷复合材料涂层为以原位生成初生相 TiC和 Cr_7C_3 为增强相、以 $(Cr,Fe)_7C_3$ 共晶为基体的复合材料涂层. 碳化物 TiC+ Cr_7C_3 均匀分布于具有优异强韧性配合及良好耐磨性的以 Cr_7C_3 和奥氏体为共晶的基体

表 2　图 3中各点成分能谱分析结果 (质量分数, %)

Table 2　EDS composition test result of each point in Fig. 3

元素	A区域	B区域	C区域
C	6.41	9.11	16.44
Cr	17.03	51.55	2.96
Mn	—	0.39	0.54
Fe	70.52	38.77	1.18
Si	2.65	—	—
Ti	3.39	—	78.89

上, 这种独特的组织赋予了涂层优异的耐磨性能, 保证了涂层在磨损过程中不开裂、不剥落, 表现出优异的耐摩擦磨损性能.

图 4为等离子熔覆 TiC/Fe-Cr金属陶瓷复合材料涂层熔合区线扫描形貌. 从图 4b中可以看出, 钛扫描线有几个跳跃点, 表明了 TiC颗粒的存在. 由铬扫描线可知, 在扫描线的 0~580 μm之间, 铬相对强度在 150以上, 且有相对宽度比较大的跳跃区, 根据前面分析, 这几个跳跃区为 Cr_7C_3区, 表明此区域是涂层区; 扫描线在 600~750 μm之间, 铬相对强度非常低, 表明此区是基材区; 而在 580~600 μm之间, 铬相对强度从 150快速下降, 跳跃性比较大, 表明此区域是涂层和基材的连接区域, 即熔合区, 由此可以确定, 熔合区的宽度为 20 μm左右.

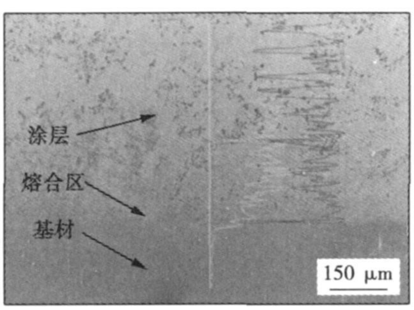

(a) 熔合区线扫描原图

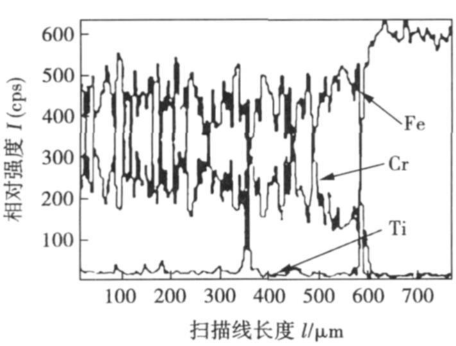

(b) 熔合区线扫描线

图 4　涂层熔合区线扫描

Fig. 4　Line scanning of elements in fusion zone

2.2　等离子熔覆 TiC/Fe-Cr金属陶瓷复合材料涂层的 TiC相的生成机理探讨

TiC晶体结构为 TiC_6或 $C\text{-}Ti_6$的正八面体, 其理想形态应为规则的八面体状. 合金中 TiC晶体形态主要受过冷度、界面能、相变熵、Ti和 C原子浓度、熔体的性质和熔体的运动状态决定的. 因此, 在高熔点的铁基合金中, TiC的生长较为复杂, 其具体形态有三种: 一种是颗粒状的多面体形态; 第二种是树枝状形态; 第三种是棒状形态. 在等离子熔覆过程中, 合金以不同的形式进入到熔池中. 一部分合金粉直接被送入到等离子弧中, 受其高温作用, 首先在过热条件下熔化, 进入熔池中; 另一部分合金粉直接进入熔池中与已熔化的基材和已熔化的合金粉混合后熔化, 当钛和碳在熔池中达到反应的浓度时, 即通过原位反应合成 TiC. 钛与碳在熔池的扩散速度差别很大, 与 Ti原子相比, C原子体积比较小, 扩散速度比较快, 所以 TiC的长大主要受限于钛的扩散.

在发生 Cr+Ti+C→TiC+Cr化学反应初期, TiC不断合成并形成晶核. 该反应是个放热反应, 结晶的同时放出大量的结晶潜热, 加快周围的钛和碳的扩散, 在已合成的晶核上合成颗粒状的 TiC. 由于颗粒状 TiC的不断形成, 周围的 Ti, C原子浓度不断降低. 但在电弧吹力、电磁搅拌等共同作用下, 熔体对流强烈, 熔体的流动, 使已合成的 TiC颗粒接触到浓度高但扩散速度慢的钛, 并不是 TiC颗粒周围都有机会接触到钛浓度高的熔液, 所以颗粒状 TiC有机会接触到高浓度的钛的那一侧, 则会在成分过冷度与温度过冷度的双重作用下, 快速生长, 长大成棒状 TiC. 已长大成棒状 TiC的不同部位也有很多机会接触到高浓度的钛, 因此这些部位也快速的生长结晶, 形成枝状 TiC. 还有一部分颗粒状 TiC由于熔体的流动冲击作用而团聚在一起, 形成团聚结构的 TiC.

2.3　等离子熔覆 TiC/Fe-Cr金属陶瓷复合材料涂层的性能分析

一般来说, 零件摩擦时, 磨损量与其接触应力、相对速度、润滑条件及摩擦副的材料有关. 而材料的耐磨性与材料硬度、显微组织有关. 因此, 提高涂层的表面硬度是提高材料性能的重要途径. 图 5为涂层沿厚度方向的显微硬度分布. 可见涂层的从表面到熔合区的硬度相差不大, 显微硬度在 740~760 HV0.2之间, 是基体金属的 3.2倍.

磨损试验结果如图 6所示, 结果表明, 等离子熔覆金属陶瓷复合材料涂层在干滑动磨损试验条件下磨损质量损失很低, 具有很好的耐磨性. 随着载荷增大, Q235钢试样磨损质量损失急剧升高, 而等离子熔覆金属陶瓷复合材料涂层磨损质量损失随载荷

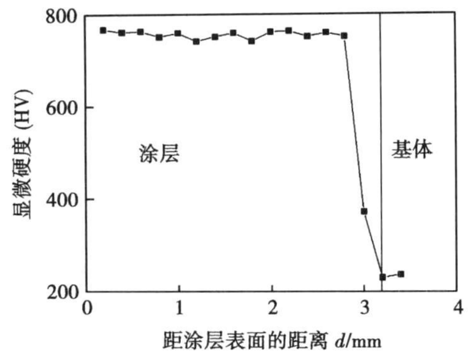

图 5　涂层沿厚度方向的显微硬度分布

Fig. 5　Microhardness (HV) of cladding layer along thickness direction

增加变化很小,对载荷变化不敏感,具有很好的载荷特性,可见,等离子熔覆金属陶瓷复合材料涂层特别适于在高接触载荷及强磨损工况下工作.

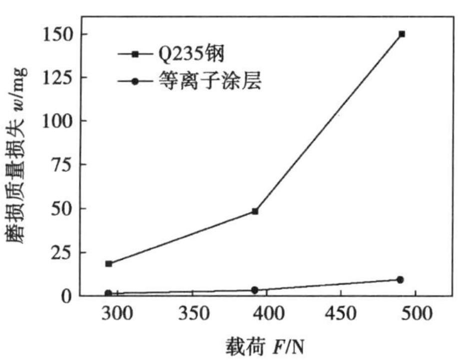

图 6　等离子熔覆涂层和 Q235钢磨损质量损失随载荷的变化

Fig. 6　Wear mass loss as a function of testing load for plasma clad composite coating as well as Q235 steel

3　结　　论

(1)以钛铁粉、高碳铬铁粉、硼铁粉、硅铁粉等为原料,利用等离子熔覆技术在 Q235钢表面原位反应合成了与基材冶金结合金属陶瓷复合涂层.

(2)涂层组织由 TiC相、初生相 Cr_7C_3、共晶相 $(Cr, Fe)_7C_3$ 和奥氏体构成. 涂层中原位合成的 TiC相呈现颗粒状、棒状和树枝状等形态,体积分数约为 21%.

(3)等离子熔覆金属陶瓷复合材料涂层显微硬度高达 760 HV0.2,约是碳钢基体的 3.2倍. 涂层磨损质量损失随载荷增加变化很小,具有很好的载荷特性.

参考文献:

[1] 单际国, 张　迪, 任家烈. 镍基合金粉末光束堆焊层的微观组织及强化机理[J]. 材料研究学报, 2002, 16(2): 151—157.
Shan Jiguo, Zhang Di, Ren Jialie. Microstructure and strengthening mechanism of Ni-based alloy powder surfacing layer by light beam[J]. Chinese Journal of Materials Research, 2002, 16(2): 151—157.

[2] Liu Y F, Mu J S, Xu X Y, et al. Microstructure and dry-sliding wear properties of TiC-reinforced composite coating prepared by plasma transferred arc weld-surfacing process[J]. Materials Science and Engineering, 2007, 58A: 366—370.

[3] Liu J B, Huang J H, Wang L M. Study on PTA clad (Cr, Fe)$_7$C$_3$/γ-Fe ceramal composite coating[J]. Acta Metallurgical Sinica (English letters), 2005, 18(6): 695—700.

[4] 杜心康, 王建江, 尹玉军, 等. 自蔓延高温合成表面涂层技术进展[J]. 材料开发与应用, 2002, 17(2): 34—38.
Du Xinkang, Wang Jianjiang, Yin Yujun, et al. Development in surface coating by self-propagating high temperature synthesis[J]. Development and Application of Materials, 2002, 17(2): 34—38.

[5] 刘均波, 王立梅, 黄继华. 反应等离子熔覆 Cr$_7$C$_3$/γ-Fe金属陶瓷复合材料涂层组织与耐磨性[J]. 焊接, 2007(1): 49—52.
Liu Junbo, Wang Limei, Huang Jihua. Microstructure and wear resistance of the reactive plasma clad Cr$_7$C$_3$/γ-Fe ceramal composite coating[J]. Welding & Joining, 2007(1): 49—52.

[6] Bedolla-Jacuinde A, Correa R, Quezada J G, et al. Effect of titanium on the as-cast microstructure of a 16% chromium white iron[J]. Materials Science and Engineering, 2005, 398(1): 297—308.

[7] Zhi Xiaohui, Xing Jiandong, Fu Hanguang, et al. Effect of titanium on the microstructure of hypereutectic high chromium cast iron[J]. Materials Characterization, 2008, 37(1): 101—104.

[8] Wang H T, Huang J H, Zhu J L, et al. Microstructure of cermet coating prepared by plasma spraying of Fe-Ti-C powder using sucrose as carbonaceous precursor[J]. Journal of Alloys and Compounds, 2009, 472(1—2): 1—5.

[9] Wang H T, Zhang S Q, Huang J H, et al. In situ TiC reinforced Ni-based composite coating prepared by flame spraying using sucrose as the source of carbon[J]. Journal of Thermal Spray Technology, 2009, 18(1): 103—109.

[10] 刘均波, 姜军生, 谭志强, 等. C/Ti原子比对前驱体碳化复合等离子熔覆 TiC/Fe复合涂层的影响[J]. 金属热处理, 2008(6): 51—53.
Liu Junbo, Jiang Junsheng, Tan Zhiqiang, et al. Influence of C/Ti atomic ratio on TiC/Fe composites coating using sucrose as a carbonaceous precursor by plasma cladding[J]. Heat Treatment of Metals, 2008(6): 51—53.

作者简介: 刘均波, 男, 1975年出生, 讲师, 博士研究生. 主要从事金属基复合材料涂层的研究工作. 发表论文 10余篇. Email: junhailiu@sina.com.cn

TiC/Cr-Fe ceramal composite coating processed by PTA

LIU Junhai[1,2], HUANG Jihua[1], LIU Junbo[3], SONG Guixiang (1. School of Materials Science and Engineering, University of Science and Technology Beijing, Beijing 100083, China; 2. Department of Mechanical and Electronic Engineering, Weihai vocational college, Weihai, Shandong 264210, China; 3. Department of Mechanical and Electronic Engineering, WeiFang University, Weifang, Shandong 261041, China; 4. Department of Vocational Skills Training Center, Weihai Vocational College, Weihai, Shandong 264210, China). p93—96

Abstract: In situ synthesized TiC particle reinforced high-chromium Fe-based composite coating was fabricated on substrate of Q235 carbon steel by plasma transferred arc (PTA) process using the mixture of ferrotitanium, ferrochromium, ferroboron and ferrosilicium powders. The microstructure and wear properties of the composite coating were investigated by means of X-ray diffraction (XRD), scanning electron micrograph (SEM), energy dispersive X-ray analysis (EDS), microhardness tester and wear tester. Results indicat that the composite coating has a rapidly solidified microstructure consisting of in-situ the reinforcing TiC carbide, primary Cr_7C_3, $(Cr,Fe)_7C_3$ eutectics, and is metallurgically bonded to the Q235 steel substrate. TiC particles present granular, rod-like and dendrite shape in the composite coating. The composite coating has high microhardness and excellent wear resistance under dry-sliding wear test condition.

Key words: plasma-transferred arc weld-surfacing; composite coating; TiC particles; Cr_7C_3; wear resistance

Analysis of microstruc ture and mechanics performance of laser buttweld for Al-Mg alloy

YAN Honghua, ZHANG Kaifeng, WU Yun (School of Materials Science and Engineering, Harbin Institute of Technology, Harbin 150001, China). p97—100, 104

Abstract: The laser buttweld of fine-grained 5083 Al alloy sheets without filler is investigated with 3 kW CO_2 laser in this paper. The influence of laser power, welding speed on the surface quality of weld is analyzed. The microstructure, mechanical properties and high temperature forming properties of welded joint are further studied. The experimental results show that the welding surface with high quality is obtained under appropriate laser power and welding speed. The profile of microhardness traverse across the weld exhibits like W shape and the heat affected zone (HAZ) has serious softening. The results of high temperature tension show that the tensile strength of welded joint is greater than the base metal, which is the side of fractures. Optimal relative height of 0.59 of the free bulging sample is obtained at 500 ℃. This result shows that laser buttwelding sheets of fine-grained 5083 Al alloy possess good high temperature formability.

Key words: aluminum alloy; laser welding; microstructure; mechanical property; formability

Influence of micro-forging on surface microstructure and cracking behavior of laser cladding layer

FAN Xiangfang, QIU Changjun, ZHOU Ju, HE Bin (School of Mechanical Engineering, University of South China, Hengyang, Hunan 421001, China). p101—104

Abstract: The accumulative effect of micro-scale plastic deformation of various frequencies can cause changes of surface microstructure and mechanical properties. Utilizing self-made machine to treat NiCrBSi laser cladding layer, OM to study geometric characteristic of plastic deformation and OM, SEM to observe influence of micro-forging on surface microstructure and cracking behavior of the laser cladding layer. It is shows that high frequency micro-forging can produce plastic deformation of about 150 microns depth onto the surface on NiCrBSi alloy clad and the dendritic crystallization microstucture which is peculiar of laser cladding layer, is broken into small pieces. Cracking susceptibility of laser cladding layer was improved greatly.

Key words: high-frequency micro-forging; laser cladding; surface microstructure; cracking behavior

Fatigue life simulation of spot weld based on equivalent structure stresses

SUN Chengzhi, CAO Guangjun (SAIC Motor Technical Center, Shanghai 201804, China). p105—108

Abstract: The fatigue life of spotwelds are predicted based on the stress-based method for tension shear and coach peel samples, the simplified beam, shell and rigid beam ware used to built the FE model of spotweld, the grid force of elements around spotweld nut ware gotten from elastic FE analysis using commercial software, the equivalent structure stresses were calculated using line force and moments, the fatigue life of spot weld of tension shear and coach peel were predicted based on master S-N curve. The physical fatigue tests have been done to valid the simulation results. The results indicted that the prediction of spotweld fatigue life based equivalent structure stresses had satisfactory approximation and could be used to predict the spotweld fatigue life of body in white in automotive industry.

Key words: fatigue life; numerical simulation; spotweld

Stress-rupture and microstructure anodysis of P92 weld joint

QIAO Yaxia, WU Yingli, GUO Jun (China Electric Power Research Institute, Beijing 100055, China). p109—112

Abstract: The P92 welded joint stress-rupture test in tension was performed at 600 ℃/10 000 h. Extrapolation the stress-rupture of P92 welded joint after 100 000 h under 600 ℃ was 116 MPa. The microstructure of P92 welded joints before and after the test were studied using metallographic microscope, TEM and EDS. The results showed that the microstructure of the welded joint was martensitem, the major precipitation $M_{23}C_6$ and high-density dislocation in transgranular. The microstructure of P92 weld joint was still lath martensite after 9395.8h stress-rupture test. The original lath was still clear, high density dislocation still exist, the new phase precipitates increase in intragranular. Furthermore, it was found that the high rupture strength of P92 weld joint was mainly due to the precipitation of $M_{23}C_6$, lath martensite and high density dislocation.

Key words: P92 weld joint; stress-rupture test; microstructure